不穩態多諧振盪器與光訊號的電磁干擾研究

蔡漢彰
正修科技大學電子工程系

陳瑞錡
正修科技大學電子工程系

摘要

本文推導不穩態多諧振盪器電磁干擾的理論公式並與實測值比較，結果相當吻合並獲結論：電磁干擾訊號其振福與頻率越大則干擾的雜訊越大，此結論也適用於雷射光訊號的電磁干擾。

關鍵詞：雜訊，諧波，不穩態振盪器，輻射能，電磁干擾，訊號雜訊比。

Investigation into EMI-induced noise in astable multivibrator and laser beam signal

Han-Chang Tsai
Department of Electronic Engineering
Chen-Shiu University

Ruey-Chyi Chen
Department of Electronic Engineering
Chen-Shiu University
No. 840, Chengcing Rd., Neausong district, Kaohsiung 83305, Taiwan

Abstract

Theoretical formulae are derived to model the time-domain and frequency-domain characteristics of the noise induced in an astable multivibrator by electromagnetic interference (EMI). The theoretical results are then compared with the experimental measurements. The experimental and numerical results reveal that the magnitude of the EMI-induced noise is related to the pulse height, the output load, the parasitic capacitance, the interference frequency and the interference amplitude. Moreover, it is shown that the harmonic noise increases with an increasing interference amplitude or interference frequency and the results of EMI are good agreements to the laser beam signal.

Keywords: Noise, Harmonic wave, Astable multivibrator, Radiated power, EMI, SNR

1. Introduction

A typical communication system contains numerous electronic components, such as resistors, filters, capacitors, multivibrators, and so forth. Moreover, a communication system comprises three main parts, namely a transmitter, a transmission channel and a receiver. The transmission channel may take various forms, including a pair of wires, a coaxial cable, a radio wave or even a laser beam. However, various undesirable effects may occur in the course of signal transmission. For example, attenuation is inevitable over long transmission distances, and leads to a reduced signal strength at the receiver end. More serious, however, are the effects of distortion, interference and noise, which appear as sudden abnormalities in the signal shape. One of the main causes of signal distortion and noise is that of electromagnetic interference (EMI) produced by the electromagnetic induction or electromagnetic radiation of an external source.

Interference may be manifested in a phenomenon known as “crosstalk” [1], in which the conversation of others can be heard when the cell phone is used, or may result in the reception of two separate radio stations at the same frequency. Furthermore, the interference produced by a cell phone (for example) may result in visual or audio distortion of a nearby television set or computer screen. In all of these examples, the intention of the original signals of the interfering device is somehow lost, and they create instead a form of electromagnetic pollution, which can result in unanticipated and undesirable effects. When electronic components are designed, it is necessary to develop high quality products capable of functioning successfully in complicated EMI-influenced environments [2-3] without themselves inducing interference in other nearby electronic appliances. Consequently, the literature contains many investigations, both experimental and theoretical, into the modeling

and suppression of EMI in numerous common applications [4-14].

The present study performs an investigation into the EMI-induced noise spectrum of a conducting wire (CW) in an astable multivibrator (AM). In a normal indoor environment, the intensity of the low-frequency electromagnetic waves is greater than that of the high-frequency electromagnetic waves (e.g., 0.03 μT and 0.0067 μT, respectively). Thus, the present study mainly focuses on the effects of low-frequency EMI on the response of the AM. Theoretical formulae are derived to model the time-domain and frequency-domain characteristics of the noise spectrum. The theoretical results are then compared with experimental measurements.

2. Interference Theory

This section develops analytical models of the basic electronic circuit of the AM, the amplified EMI signal coupled into the AM via a CW, and the resulting noise spectrum, respectively. Fig. 1 and 2 show the basic electronic circuits of the AM device.

2.1 DC analysis and designed circuit

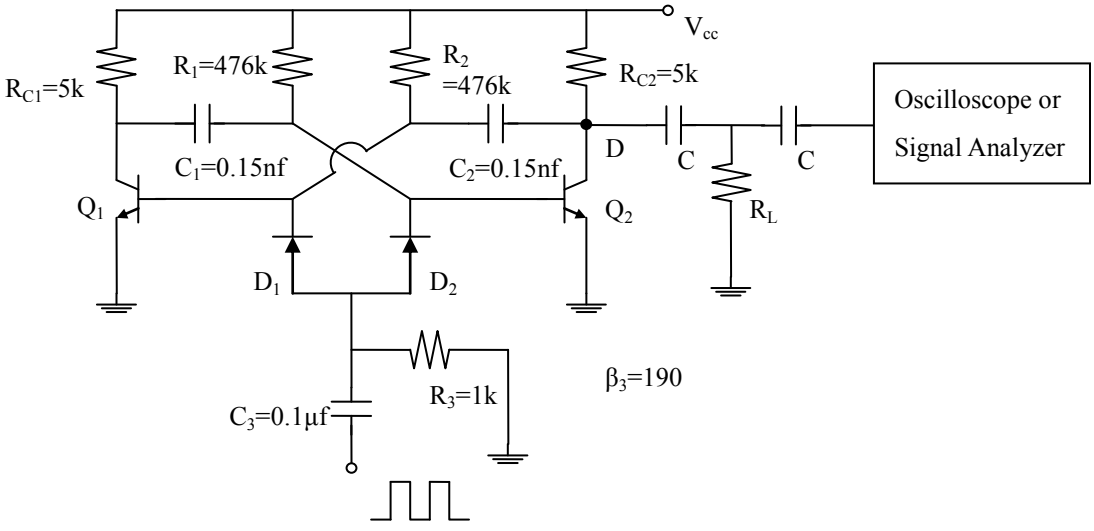

Fig. 1: Basic experimental circuit.

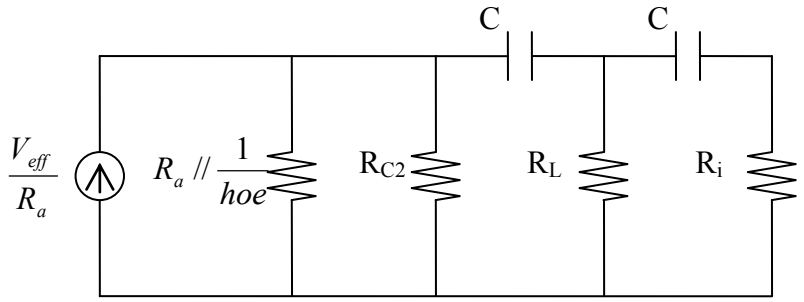

Fig. 2: Output circuit used for AC analysis.

In Fig. 1, the differential circuit (R_3 and C_3) is designed to change the output frequency of the basic circuit. Since the elements are not completely symmetric in the circuit, when V_{CC} (experimental V_{CC} =3 V) is plugged in, if Q_1 is switched on and Q_2 is switched off, then V_{CE1} is equal to 0.2 V. Moreover, if the circuit is in a stable state, V_{C2} will be charged initially to 2.1 V and will then discharge. For the loop containing V_{CC}, R_1, C_1 and V_{CE1}, when C_1 is recharged, the base voltage of Q_2 becomes positive and increases gradually until Q_2 switches on. The voltage V_{CE2} then reduces from 2.8 V to 0.2 V. From the preceding discussions, it follows that

$$V_{CE2(off)} = 2.1 + V_{BE1} = 2.1 + 0.7 = 2.8 . \quad (1)$$

Meanwhile, the voltage V_{BE1} is given by

$$V_{CE2} - V_{C2} - V_{BE1} = 0 , \quad (2)$$

$$V_{BE1} = 0.2 - 2.1 = -1.9 . \quad (3)$$

Thus, Q1 turns off for a short time.

As for the case of a monostable multivibrator, the charge and discharge times of the capacitors in an AM are given by

$$T_1 = 0.693 R_1 C_1, \text{ for } Q_1 \text{ on, } Q_2 \text{ off time} \quad (4)$$

$$T_2 = 0.693 R_2 C_2, \text{ for } Q_2 \text{ on, } Q_1 \text{ off time} \quad (5)$$

When $R_1 = R_2, C_1 = C_2$, the square wave period, T_{AM}, is expressed as

$$T_{AM} = T_1 + T_2 = 0.693(R_1C_1 + R_2C_2) = 1.386RC \quad . \tag{6}$$

For Q_1 on, Q_2 off time For Q_2 on, Q_1 off time

Design

1. If R_1=476k, and T_{AM}=0.1ms (i.e., f_{AM}=10 kHz), then

$$C_1 = \frac{0.0001}{1.386 \times 476k} = 151.6 \times 10^{-12} f \text{ . Take } C_1\text{=150 pf.} \tag{7}$$

2. $\beta I_{B1} > I_{C1(sat)}$, (8)

$$I_{C1(sat)} = \frac{V_{CC} - 0.2}{R_{C1}}, \tag{9}$$

$$I_{B1} = \frac{V_{CC} - 0.7}{R_2} == \frac{2.3}{476.19k} = 0.0048mA, \tag{10}$$

$$\beta I_{B1} = 190 \times 0.0048mA \geq I_{C1(sat)} = \frac{3 - 0.2}{R_{C1}} = \frac{2.8}{R_{C1}}, \tag{11}$$

$$R_{C1} \geq \frac{2.8}{190 \times 0.0048mA} = 3070\Omega, \text{ take } R_{C1}\text{=5k=}R_{C2}. \tag{12}$$

2.2 EMI coupling analysis

The interference source considered in the present study has the form of a coil wound on a ferromagnetic toroid containing an air gap. A CW is positioned in the air gap and induces an EMI voltage of magnitude V_{eff} when a current is passed through the coil. Moreover, the magnetic field in the air gap also induces a current in the CW. This current is amplified by a 73.98 dB low-noise pre-amplifier so that it can be detected by an oscilloscope and is then connected with the AM in series. The resulting EMI interference is detected initially as radiated noise and is then coupled in series into the AM in the form of conducted noise. The EMI signals are transmitted to the

oscilloscope via the circuit coupling and are then passed to a spectrum analyzer in order to generate the time-domain and frequency-domain plots of the interference signals.

In performing the present experiments, the EMI frequency was varied in the range of 300 Hz to 1 kHz, while the amplitude of the interference was varied between 0.3 V and 1.0 V. The experimental system was shielded within a metal case in order to suppress the effects of external noise. The amplifier and current source were both powered by batteries. In addition, the signal analyzer (HP E4440A) was controlled by a PC via an IEEE-488 bus. The magnetic field density and flux density generated in the air gap of the ferromagnetic toroid are given respectively as [15]

$$H_g = \frac{\mu N I_0}{\mu_0 (2\pi r_0 - \lambda_g) + \mu \lambda_g}, \tag{13}$$

$$P_{rB} = \frac{1}{2}\int \mu_0 H_g{}^2 dv = \frac{1}{2}\int H_g B_g dv, \tag{14}$$

where μ_0 is the permeability of free space, μ is the permeability of the ferromagnetic material, I_0 is the intensity of the current flowing through the coil, r_0 is the mean radius of the toroid, lg is the width of the air gap, and P_{rB} is the magnetic energy in the air gap. Note that P_{rB} represents the average energy per second of the interference on the CW, and can be either calculated or measured directly. Fig. 3 shows the equivalent circuit of the ferromagnetic toroid.

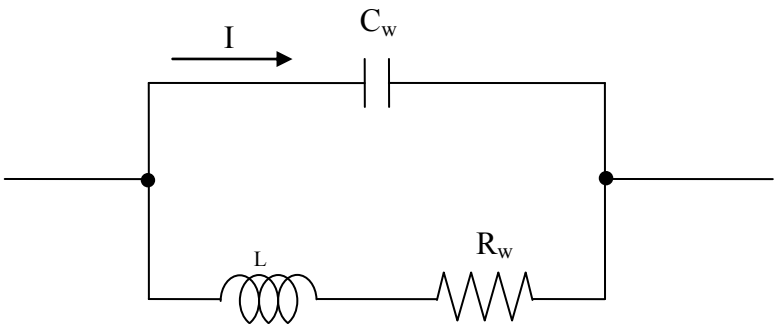

Fig. 3: Equivalent circuit of ferromagnetic toroid.

In general, any periodic signal can be represented by the following complex Fourier series:

$$V(t)=\sum_{n=-\infty}^{\infty}C_n e^{jn\omega t}=C_0+\sum_{n=1}^{\infty}2\left|C_n\right|\cos\left(n\omega t+\angle C_n\right) \tag{15}$$

.

In the present study, the input signal of the ferromagnetic toroid has the form of a periodic square wave (see Fig. 4). Hence, the following Fourier transform applies:

$$C_n=\frac{1}{T}\int_0^{t_0}V_0(t)e^{-jn\omega t}dt=\frac{V_0t_0}{T}\frac{\sin\frac{1}{2}n\omega t_0}{\frac{1}{2}n\omega t_0}e^{-j\frac{1}{2}n\omega t_0}. \tag{16}$$

Let

$$K_n=\frac{V_0t_0}{T}\frac{\sin\frac{1}{2}n\omega t_0}{\frac{1}{2}n\omega t_0}, \tag{17}$$

$$\angle C_n=\frac{1}{2}n\omega t_0 . \tag{18}$$

Substituting Eqs. (17) and (18) into Eq. (15) gives

$$V(t)=\frac{V_0}{2}+\sum_{n=1}^{\infty}K_n\cos\left(n\omega t_0+\frac{n\pi}{2}\right),\ \text{for}\ \ t_0=\frac{T}{2}. \tag{19}$$

In Fig. 3, the following admittance can be obtained:

$$Y=\frac{\left(R_\omega+jn\omega L\right)+\dfrac{1}{jn\omega C_\omega}}{\left(R_\omega+jn\omega L\right)\dfrac{1}{jn\omega C_\omega}}=\frac{1}{{R_\omega}^2+n^2\omega^2L^2}\left[R_\omega+j\left(n\omega R_\omega^2C_\omega-n\omega L+n^3\omega^3L^2C_\omega\right)\right]$$

$$=\left|Y\right|\angle\theta_1\ . \tag{20}$$

$$I=YV(t)=C_0Y_0+\sum_{n=1}^{\infty}2K_n\left|Y\right|\cos\left(n\omega t+\angle C_n+\theta_1\right) \tag{21}$$

.

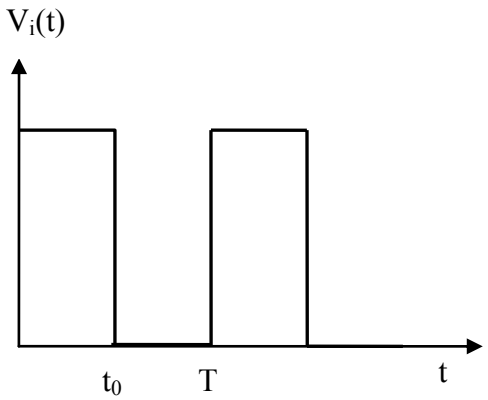

Fig. 4: Square wave electromagnetic interference signal acting on ferromagnetic toroid.

From Eq. (13), it can be shown that

$$V_{eff}=-\frac{1}{dt}\int_s\vec{B}\cdot d\vec{s}=-\frac{1}{dt}\left[\frac{\mu_0\mu NI}{\mu_0\left(2\pi r_0-l_g\right)+\mu l_g}\cdot\Delta zd\right] \tag{22}$$

$$=\frac{\mu_0\mu N\left(\Delta zd\right)}{\mu_0\left(2\pi r_0-l_g\right)+\mu l_g}\sum_{n=1}^{\infty}2K_n\left|Y\right|n\omega\sin\left(n\omega t+\angle C_n+\theta_1\right) \tag{23}$$

$$=\sum_{n=1}^{\infty}2KK_n\left|Y\right|n\omega\sin\left(n\omega t+\angle C_n+\theta_1\right)$$

,

$$K=\frac{\mu_0\mu N\Delta zd}{\mu_0\left(2\pi r_0-l_g\right)+\mu l_g}\ , \tag{24}$$

where Δz is the interfered length of the CW. In Fig. 2, the signal output to the oscilloscope or signal analyzer, V_{out}, has the form

$$V_{\text{out}} = V_{\text{eff}} \frac{K_1}{R_a} \cdot \frac{K_3 \angle \theta_3}{K_2 \angle \theta_2} \cdot \frac{R_i}{K_4 \angle \theta_4}, \tag{25}$$

where R_i is the input resistance of the measured appliance, and $K_1=R_a//(1/h_{oe})// R_{C2}$ for a small value of C_{ce}.

$$Q_2 = K_1 - j\frac{1}{\omega C} = K_2 \angle \theta_2, \tag{26}$$

$$K_2 = \left[K_1^{\,2} + \left(\frac{1}{\omega C} \right)^2 \right]^{\frac{1}{2}},$$

$$\theta_2 = \tan^{-1} \frac{-\frac{1}{\omega C}}{K_1}, \tag{27}$$

$$Q_3 = K_2 \angle \theta_2 \,//\, R_L = K_3 \angle \theta_3 = a + bj, \tag{28}$$

$$K_3 = \frac{1}{(K_1 + R_L)^2 + \left(\frac{1}{\omega C} \right)^2} \left\{ \left[K_1 R_L (K_1 + R_L) + \frac{R_L}{\omega^2 C^2} \right]^2 + \left[\frac{K_1 R_L}{\omega C} - (K_1 + R_L) \frac{R_L}{\omega C} \right]^2 \right\}^{1/2}$$

$$\theta_3 = \tan^{-1} \frac{\frac{K_1 R_L}{\omega C} - (K_1 + R_L) \frac{R_L}{\omega C}}{K_1 R_L (K_1 + R_L) + \frac{R_L}{\omega^2 C^2}}, \tag{29}$$

$$Q_4 = (K_1 + X_C) // R_L + X_C + R_i = Q_3 + X_C + R_i$$
$$= a + R_i + j\left(b - \frac{1}{\omega C} \right),$$

$$= K_4 \angle \theta_4 \tag{30}$$

$$K_4 = \left[(a + R_i)^2 + \left(b - \frac{1}{\omega C} \right)^2 \right]^{\frac{1}{2}},$$

$$\theta_4 = \tan^{-1} \frac{b - \frac{1}{\omega C}}{a + R_i}. \tag{31}$$

From the above, it can be shown that

$$V_{\text{out}} = \sum_{n=1}^{\infty} \frac{2KK_n |Y| n\omega K_1 K_3 R_i \sin(n\omega t + \angle C_n + \theta_1 + \theta_3 - \theta_2 - \theta_4)}{R_a K_2 K_4} \quad , \tag{32}$$

$$V_{\text{out}} = \sum_{n=1}^{\infty} \frac{C_5 KK_n |Y| n\omega K_1 K_3 R_i \sin(n\omega t + \angle C_n + \theta_1 + \theta_3 - \theta_2 - \theta_4)}{R_a K_2 K_4} \quad , \tag{33}$$

where C_5 is the effective induction coefficient.

2.3 Noise analysis

When a current is passed through the wire wrapped around the ferromagnetic toroid, the CW in the air gap induces a pulse voltage in the transistor circuit, which in turn generates a noise spectrum in the AM. Fig. 5 shows the typical response wave acquired by the oscilloscope for a periodic pulse of period T. Note that the figure shows both the experimental results and the numerical results for comparison

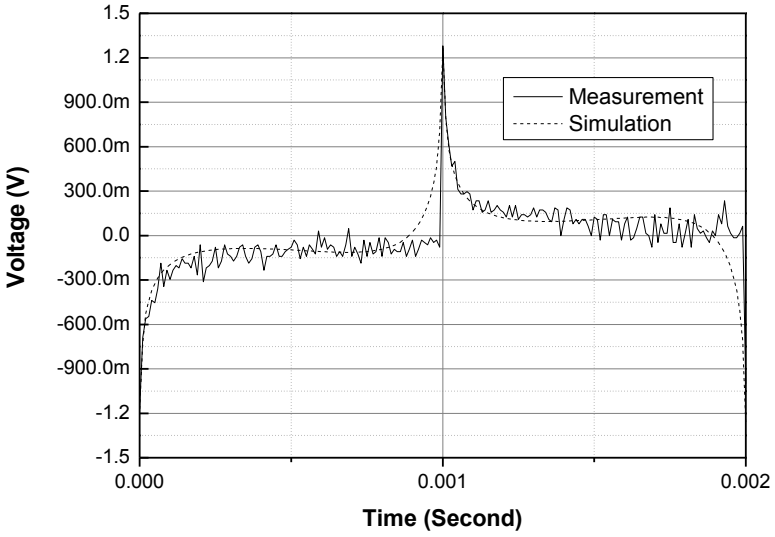

Fig. 5: Measurement and simulation results for typical periodic pulse function generated by periodic EMI signal with period T.

purposes. The response pulse can be analyzed by taking the discrete Fourier transformation of function A (the pulse height), i.e.,

$$S_n = \frac{1}{T}\left[\int_{-T_0}^{0} -A_1 e^{-a(T_0+t)} e^{-j\omega nt} dt + \int_{0}^{T_0} A_2 e^{-at} e^{-j\omega nt} dt\right]$$

$$= \frac{1}{T}\frac{a - j\omega n}{a^2 + \omega^2 n^2}\left[E - jD\right] \ , \tag{34}$$

where

$$E = A_1 e^{-aT_0} + A_2 - A_2 e^{-aT_0}\cos \omega n T_0 - A_1 \cos \omega n T_0 \ , \tag{35}$$

$$D = -A_2 e^{-aT_0}\sin \omega n T_0 + A_1 \sin \omega n T_0 \ , \tag{36}$$

$$S_n{}^2 = \frac{1}{T^2(a^2 + \omega^2 n^2)}\left[E^2 + D^2\right] \ . \tag{37}$$

Note that in the equations above, n is an integer, $\omega = 2\pi f = 2\pi/T$, a is the attenuation factor of the exponential function, and A (i.e., A_1 or A_2) is the amplitude of the EMI signal induced by the CW. The amplitude spectrum of the EMI current can be obtained by plotting S_n against the discrete frequencies, ωn. Note that the square of S_n has dimensions of A^2 and corresponds to the current power spectrum $S_{i\lambda}(f_n)$ over a duration 2T [16].

Regarding the parasitic capacitance, the Norton equivalent output circuit has the form shown in Fig. 6. Let $V_{ce}=V_C$ and $C_{ce}=C$. Thus, it can be shown that

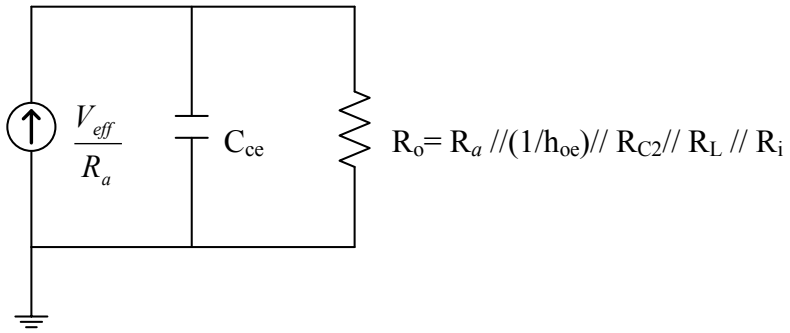

Fig. 6: Simplified representation of EMI output port in Fig. 2.

$$i_n = i_C + i_0 = C\frac{d\Delta V_C}{dt} + \frac{\Delta V_C}{R_0} \Rightarrow \frac{d\Delta V_C}{dt} + \frac{\Delta V_C}{R_0 C} = \frac{i_n}{C} \ , \tag{38}$$

where $R_0 = R_a \,//\, 1/h_{oe} \,//\, R_{c2} \,//\, R_L \,//\, R_i$, and ΔV_c is the variation in the voltage across the capacitor. Taking the Fourier series expansions of ΔV_c and i_n gives

$$\frac{i_n}{C} = \frac{1}{C}\sum_{n=-\infty}^{\infty}\alpha_n \exp(j\omega_n t) \ , \tag{39}$$

$$\frac{d(\Delta V_{cn})}{dt}+\frac{\Delta V_{cn}}{R_0C}=\frac{1}{C}\alpha_n\exp(j\omega_n t)\,. \tag{40}$$

Thus, it can be shown that

$$\Delta V_{cn}=\beta_n\exp(j\omega_n t), \tag{41}$$

where

$$\beta_n=\frac{\alpha_n R_0}{1+j\omega_n R_0 C}\,. \tag{42}$$

As a result, the noise power spectrum, $S_{\Delta Vc}(f_n)$, of the voltage induced by the EMI signal is given by

$$S_{\Delta Vc}(f_n)=2T\overline{\beta_n\beta_n^{\pi}}\,, \tag{43}$$

$$S_{\Delta Vc}(f_n)=S_{i\lambda}(f_n)\frac{{R_0}^2}{(1+\omega nR_0C)^2}\,, \tag{44}$$

where:

$$S_{i\lambda}(f_n)=2T\overline{\alpha_n\alpha_n^{*}}=2T{S_n}^2\,. \tag{45}$$

From Eqs. (34) and (40), it can be shown that

$$S_{\Delta V_C}(f_n)=2T\frac{{R_0}^2}{1+(\omega_1 nR_0C)^2}\left[\frac{1}{T^2(a^2+\omega^2n^2)}(E^2+D^2\right]. \tag{46}$$

The total noise power can be obtained by summing $S_{\triangle Vc}(f_n)$ over all possible integers, *n*. To identify the relative magnitudes of the various harmonic components, the current analysis commences by finding the value of A (i.e., the pulse height) from the measured power spectral intensity of the fundamental harmonic and then evaluates the power spectral intensities of the higher-order harmonics. Adopting this approach, the experimental response wave shown in Fig. 5 can be transformed directly into the noise spectrum presented in Fig. 7. Equations (33) and (46) reveal that the magnitude of the EMI-induced noise is governed by the pulse height, the output load, the parasitic capacitance, the interference frequency and the interference amplitude.

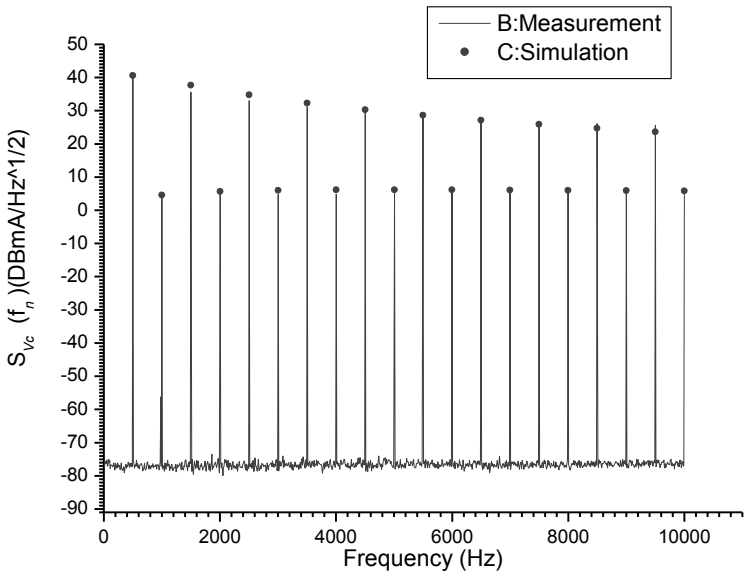

Fig. 7: Typical noise spectrum response.

The basic output frequency of an AM circuit has the form of a sine wave. Generally speaking, the effects of the 10 kHz basic output frequency on the noise power spectrum of the AM can be mitigated using an impedance-matching method. Fig. 8(a) shows the output equivalent circuit of the EMI signal passed to the oscilloscope or signal analyzer, where $R_{O1}=1/h_{oe}$ //R_{C2}// R_L// R_i=49.41 Ω. Meanwhile, Fig. 8(b) shows the output equivalent circuit of the basic oscillating sine wave of the AM, where $R_{O2}=1/h_{oe}$ //R_a// R_L// R_i=24.98 Ω. The output powers of the EMI and basic AM signals are given respectively by

$$P_{EMI} = (\frac{V_{eff}}{50+49.41})^2 49.41 = 0.005(V_{eff})^2 . \quad (47)$$

$$P_{AM} = (\frac{V_{AM}}{5^k+24.98})^2 24.98 = 9.9\times10^{-7}(V_{AM})^2 . \quad (48)$$

From Eqs. (47) and (48), it can be seen that P_{AM}/P_{EMI}=1.98E-4. In other words, the basic output power of the AM is negligible compared to that of the EMI-induced signal and can therefore be ignored.

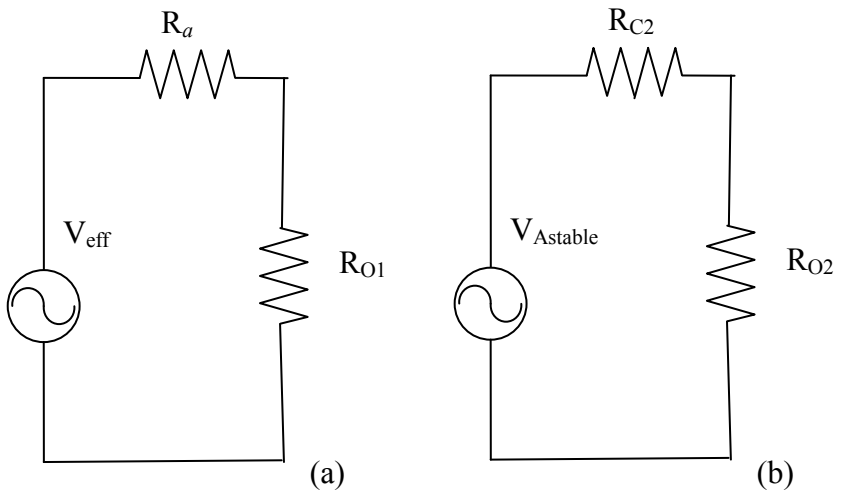

Fig. 8: Output equivalent circuits of (a) EMI signal and (b) AM signal.

3. Results and Discussion

As described above, Fig. 5 shows a typical pulse function generated by a periodic EMI signal with a period T. Using Eq. (33), the following parameter values were assumed: V_0=1.17 V (at time t=0), V_0=1.28 V (at time t=T/2), μ_0=4πE-7 H/m, μ_r=4000, N=500, F=500 Hz, R_ω=0.52 Ω, r_0=0.09 m, l_g =0.005 m, R_a=50 Ω, C_ω=6.558E-10 F, C=220E-6 F, Δz=0.01 m, d=0.001 m, $1/h_{oe}$=30 KΩ, R_{c2}=5 kΩ, C_5=0.155, X_C=1/(2π*f*C), R_L=220 KΩ, L=1E-4 H, C_{ce}=12.77E-8 F, R_L=220KΩ, T_0=0.4981T, *f*=500 Hz, ω=2π*f* and R_i=50Ω. It is shown in Fig. 5 that a good qualitative agreement exists between the simulation results and the corresponding measurement results. In simulating the noise spectrum of the interfered AM using Eq. (46), the attenuation factor of the exponential function was assigned a value of a=8622. Fig. 7 presents the experimental results obtained for the noise spectrum induced by an EMI signal in the form of a square wave with an amplitude of V_P=1.0 V and a frequency of *f*=500 Hz. Having obtained the experimental noise spectrum, an experimental data point was selected in order to inversely derive the amplitudes A_1 and A_2 of the corresponding EMI current. Applying a fitting technique, A_1 and A_2 were

determined to be A_1=310.88 mA and A_2=318.78 mA, respectively. A good agreement is observed between the two sets of results (see Fig. 7). To further investigate the effect of EMI on the noise spectrum induced in the AM, the amplitude of the AC interference signal was varied in the range of 0.3~1.0 V while the interference frequency was maintained at a constant value of f=500 Hz. Fig. 9 compares the corresponding experimental and simulation results for the odd-order harmonic components in the noise spectrum. Note that the simulated values of A_1 range from 91.86 mA to 310.88 mA, while the values of A_2 range from 94.19 mA to 318.78 mA. In all cases, a good agreement is observed between the simulation results and the experimental data.

Table 1 compares the measured and simulated values of the maximum noise power spectral intensity induced by a square-wave EMI signal with a constant frequency of *f*=500 Hz and various amplitudes in the range of V_p= 0.3 ~ 1.0 V. Meanwhile, Table 2 compares the experimental and simulation results obtained for the maximum noise power spectral intensity given a square-wave EMI signal with various frequencies in the range of *f* = 300~1000 Hz and an amplitude of V_p= 1.0 V.

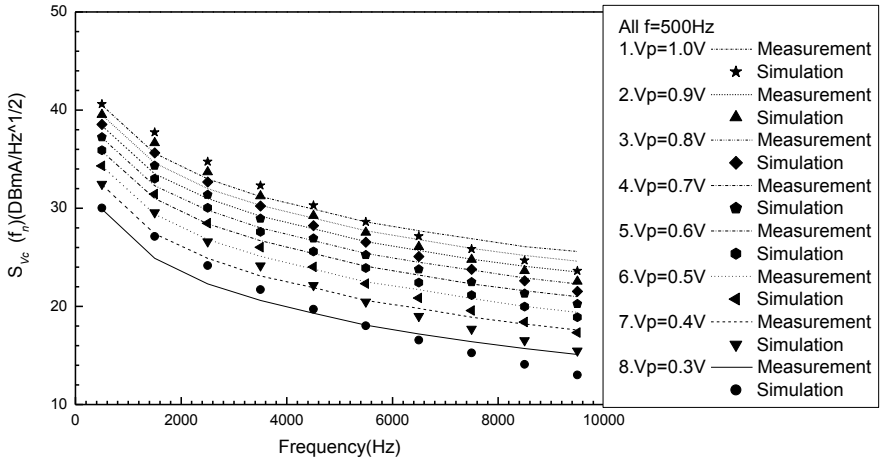

Fig. 9: Experimental and simulation results for odd-order harmonics of noise spectrum induced by EMI interference with frequency of 500 Hz and amplitude of V_p= 0.3 V to 1.0 V.

Fig. 10 presents the experimental and simulation results obtained for the odd-order harmonic components of the noise spectrum as a function of the interference frequency. Although a -3 dB difference is observed between the two sets of results, the significant effect of the EMI frequency on the induced noise is clear in both cases. By tuning the amplitude and frequency parameters, then the same accuracy as that shown in Fig. 9 can be obtained in Fig. 11 and Table 3. Fig. 9 shows the difference between the experimental and simulation results for the variable amplitude

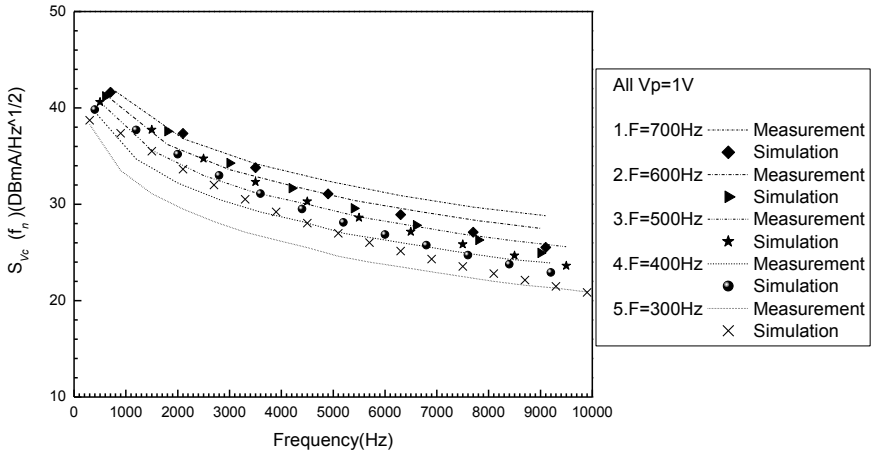

Fig. 10: Experimental and simulation results for odd-order harmonics of noise spectrum induced by EMI interference frequency of 300~700 Hz and amplitude of V_p= 1V.

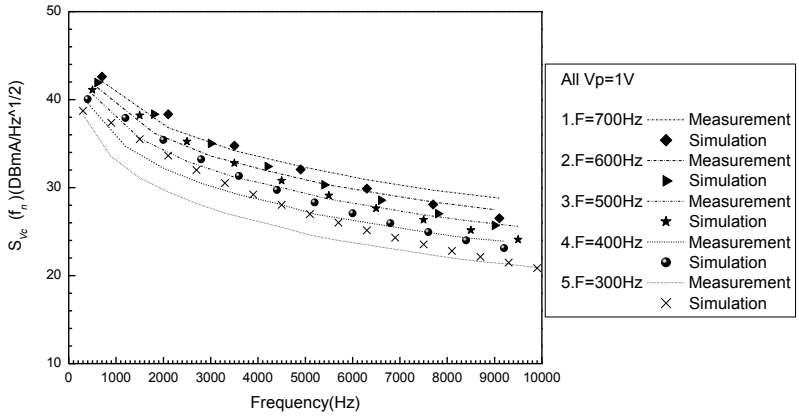

Fig. 11: Experimental and simulation results for odd-order harmonics of noise spectrum induced by EMI interference frequency of 300~700 Hz with

table 3.

case that is less than that for the variable frequency case. In other words, the effect of the EMI amplitude is more significant than that of the EMI frequency.

In general, the simulation and experimental results presented above indicate that the magnitude of the EMI induced by the CW varies as a function of the amplitude, frequency and period of the interference signal. The magnitude of the EMI is also affected by the collector resistance, the parasitic capacitance of the AM, the output load and the attenuation factor of the exponential function. Table 4 indicates the signal-to-noise (SNR) ratio of the AM for a reference signal of Si = 100 μA and various values of the interference amplitude.

In the experimental setup used in the present study, the CW has a length of 1 cm. However, the length of the CW in a practical electrical circuit may exceed 1 m, and thus the EMI effect may potentially be magnified by a factor of 5000 times relative to that predicted in the current results. This will clearly have a significant effect on the circuit; particularly if the EMI is induced at the receiving terminal of a communication system. Assuming an induced current of 36.632 μA, a CW of length 1 cm, and a load resistance of 49 Ω, the induced voltage is 1795 μV, which may be amplified by around 100 times in a practical system. According to EN55022 (European Standard) and CISPR 11 (International Special Committee on Radio Interference), EMI should be limited to no more than 110 dBμV in the interference frequency range of 0.009~0.050 MHz (equivalent to a voltage of 316228 μV). To satisfy these conditions, the length of the CW in the system should be no longer than 1.76 cm. By the way, as shown in the following, the basic results developed in this study can also be applied to the case of optical signal (wave length=632 nm)

interference. In Fig. 12, the electromagnetic wave is modeled a hollow PVC tube wrapped with a current-carrying coil, while the detector has the form of a PIN (Positive-Intrinsic-Negative) photodiode. Fig. 13 shows the Effect of forward DC interference voltage V_P on detected voltage waveform. Input voltage to A1 and B1 varies in the range of $V_P = 0V \sim 0.6V$ with step $\Delta V_p = 0.1V$. Note that the direction of the induced magnetic field is the forward of that of the laser beam. It is seen that as

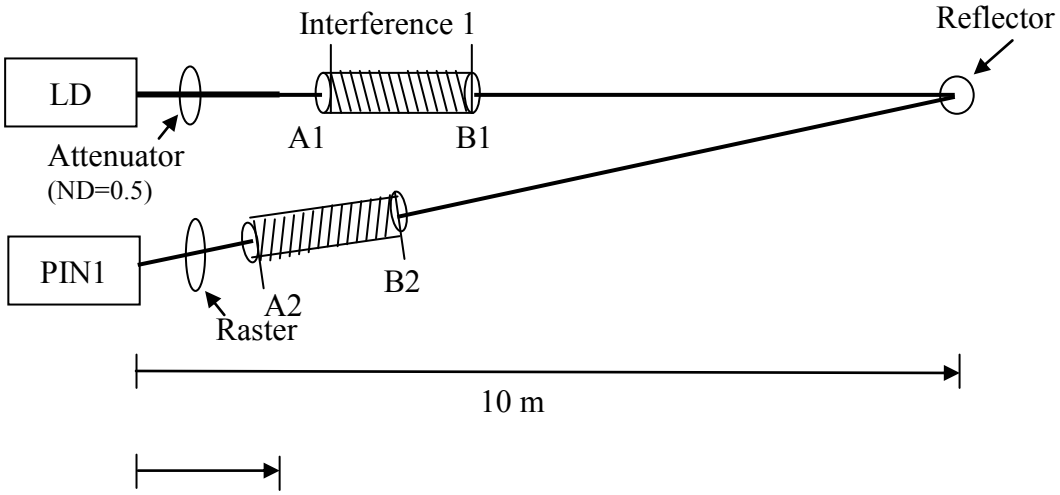

Fig. 12: Experimental setup for EMI spectrum measurement.

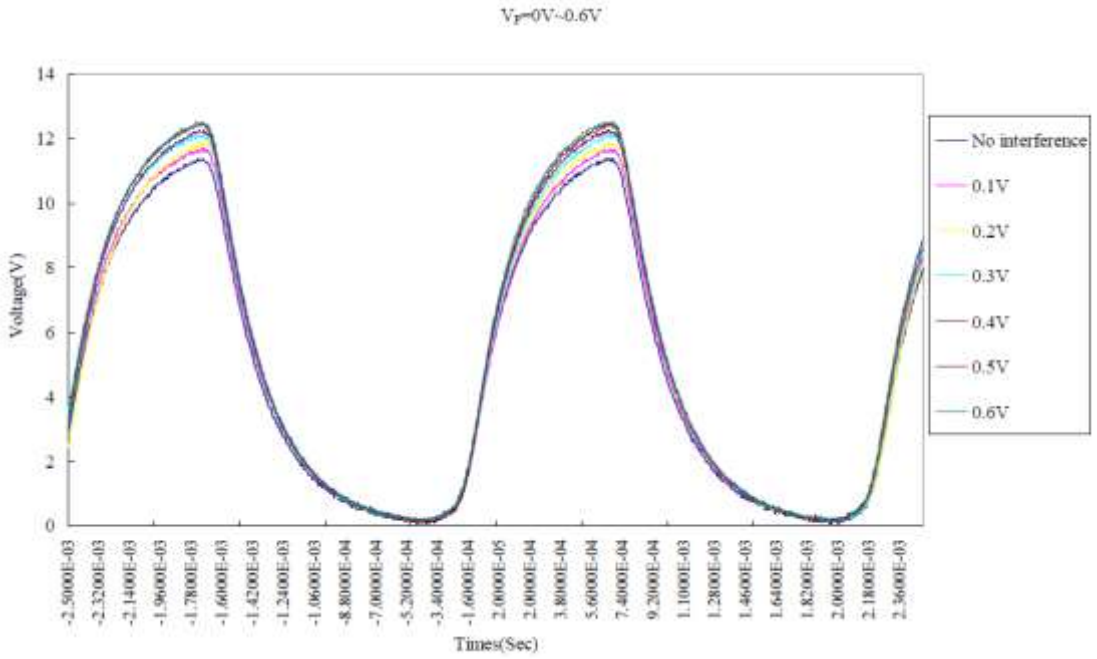

Fig. 13：Effect of forward DC interference voltage V_P on detected voltage waveform.

the amplitude of the interference voltage increases, the intensity of the detected light signal also increases.

4. Conclusions

This study has employed a combined theoretical and experimental approach to characterize the noise spectrum of an astable multivibrator (AM) interfered with by a periodic EMI signal coupled into the AM via a conducting wire. In general, a good agreement has been observed between the measured interference results and the simulation results in both the time domain and the frequency domain. Overall, the results have indicated that the effect of the EMI on the AM is governed by parameters f, V_0, μ_0, μ_r, N, R_ω, r_0, l_g, R_a, C_ω, C_{ce}, R_i, Δz, d, R_c, L, A_1, A_2, a, T_0, R_L and C, and the radiated power. Furthermore, it has been shown that the magnitude of the induced interference current increases as the frequency and amplitude of the interference signal increases. Of the two interference characteristics, the amplitude exerts a greater

effect on the induced noise spectrum than the frequency. In accordance with CISPR and EN norms, the results presented in this study imply that the conducting wires used in practical electronic circuits should not exceed a length of 1.76 cm.

This study has considered the particular case of an AM. However, adapting the basic theorems developed in this study is a convenient approach to conducting the EMI analysis of all similar wavelength-based electronic devices, such as the laser beam signal.

Acknowledgement

The author wishes to acknowledge the invaluable assistance provided by Haw-Jiun Liang throughout the course of this study.

References

1. B. Liu, L. Cai, P. Bai, W. Peng, Reliability evaluation for single event crosstalk via probabilistic transfer matrix, Microelectronics Reliability, 52 (2012) 1511-1514.
2. O. Aiello, F. Fiori, A new MagFET-based integrated current sensor highly immune to EMI, Microelectronics Reliability, 53 (2013) 573-581.
3. J. Missinne, E. Bosman, B. V. Hoe, R. Verplancke, G.V. Steenberge, S. Kalathimekkad, P.V. Daele, J. Vanfleteren, Two axis optoelectronic tactile shear stress sensor, Sensors & Actuators A: Physical, 186 (2012) 63-68.
4. Ji Qing, Xinbo Ruan, Zhihong Ye, The Worst Conducted EMI Spectrum of Critical Conduction Mode Boost PFC Converter, IEEE Transactions on Power Electronics, 30 (2015) 1230-1241.
5. ZHOU Qiuzhan, CHEN Yongzhi, YOU Ziyue, Infrastructure-Mediated Sensing Based Home Appliances Monitoring System Using the EMI Characteristics, Chinese Journal of Electronics, 23 (2014) 586-590.
6. Lukovic, M.D., Nikolic, M.V., Blaz, N.V., Zivanov, L.D., Aleksic, O.S., Lukic, L.S., Mn-Zn Ferrite Round Cable EMI Suppressor With Deep Grooves and a Secondary Short Circuit for Different Frequency Ranges, IEEE Transactions on Magnetics, 49 (2013) 1172-1177.

7. N. Joseph, S.K. Singh, R.K. Sirugudu, V.R.K. Murthy, S. Ananthakumar, M.T. Sebastian, Effect of silver incorporation into PVDF-barium titanate composites for EMI shielding applications, Materials Research Bulletin, 48 (2013) 1681-1687.
8. J. Chen, Z. Du, Device simulation studies on latch-up effects in CMOS inverters induced by microwave pulse, Microelectronics Reliability, 53 (2013) 371-378.
9. M. Tlig, J. Ben Hadj Slama, M.A. Belaid, Conducted and radiated EMI evolution of power RF N-LDMOS after accelerated ageing tests, Microelectronics Reliability, 53 (2013) 1793-1797.
10. C.K. Jang, J.H. Park, J.Y. Jaung, MWNT/PEG grafted nanocomposites and an analysis of their EMI shielding properties, Materials Research Bulletin 47 (2013) 2767-2771.
11. H.R. Kim, K. Fujimori, B.S. Kim, I.S. Kim, Lightweight nanofibrous EMI shielding nanowebs prepared by electrospinning and metallization, Composites Science and Technology 72 (2013) 1233-1239.
12. A. Kaur, Ishpal, S.K. Dhawan, Tuning of EMI shielding properties of polypyrrole nanoparticles with surfactant concentration, Synthetic Metals 162 (2013) 1471-1477.
13. G. Groos, Characterisation method for chip card ESD events causing terminal failures, Microelectronics Reliability, 52 (2013) 2005-2009.
14. H. Guo, H. Wu, B. Zhang, Z. Li, A novel spread-spectrum clock generator for suppressing conducted EMI in switching power supply, Microelectronics Journal, 41 (2010) 93-98.
15. D.K. Cheng, Field and wave electromagnetics. 2nd ed. USA: Addison-Wesley Publishing Company; 1989. pp. 252-280.
16. Aldert van der Ziel, “Noise in solid state devices and circuits”, New York: Wiley, 1986, pp. 10, 19.

Table 1: Comparison of experimental and theoretical results for maximum noise power spectral intensity for various values of interference amplitude.

Frequency fixed , Amplitude variable (First harmonic wave)								
Vp(V)	0.3	0.4	0.5	0.6	0.7	0.8	0.9	1.0
Frequency (Hz)	500	500	500	500	500	500	500	500
Induced Current A1(A)	0.09186	0.12182	0.15083	0.18084	0.21085	0.24486	0.27487	0.31088
Induced Current A2(A)	0.09419	0.12492	0.15471	0.18548	0.21624	0.25110	0.28186	0.31878
Measurement ($dBmA/Hz^{1/2}$)	29.9	32.4	34.3	35.8	37.2	38.4	39.5	40.6
Simulation ($dBmA/Hz^{1/2}$)	30.01	32.47	34.33	35.90	37.23	38.53	39.54	40.61

Table 2: Comparison of experimental and theoretical results for maximum noise power spectral intensity for various values of interference frequency.

Amplitude fixed , Frequency variable (First harmonic wave)								
Frequency(Hz)	300	400	500	600	700	800	900	1000
Measurement ($dBmA/Hz^{1/2}$)	38.3	39.6	40.6	41.4	42.1	42.6	43.1	43.6
Simulation ($dBmA/Hz^{1/2}$)	38.72	39.82	40.61	41.18	41.62	41.95	42.21	42.42

Table 3: Comparison of experimental and theoretical results for maximum noise power spectral intensity for various values of interference frequency and amplitude.

Amplitude , Frequency variable (First harmonic wave)					
Frequency(Hz)	300	400	500	600	700
Induced Current A1 (A)	0.31088	0.31868	0.32888	0.33888	0.34826
Induced	0.31878	0.32678	0.33724	0.34749	0.35711

Current A2 (A)					
Measurement ($dBmA/Hz^{1/2}$)	38.3	39.6	40.6	41.4	42.1
Simulation ($dBmA/Hz^{1/2}$)	38.72	40.04	41.09	41.93	42.61

Table 4: Relative SNR of current induced by EMI.

V_P (V)	0.3	0.4	0.5	0.6	0.7	0.8	0.9	1.0
Induced Current A1(A)	0.09186	0.12182	0.15083	0.18084	0.21085	0.24486	0.27487	0.31088
Induced Current A2(A)	0.09419	0.12492	0.15471	0.18548	0.21624	0.25110	0.28186	0.31878
Induced Peak Current N_i (μA)	18.605	24.674	30.554	36.632	42.709	49.596	55.673	62.966
Relative SNR (dBμA)	14.607	12.155	10.299	8.723	7.390	6.091	5.087	4.019

Where $SNR=20Log(S_i/N_i)$, $S_i=100\mu A$, $N_i=((A1+A2)/2)/(5000)$ and $f=500Hz$.